



Ruddlesden Popper oxide of $\text{LnSr}_3\text{Fe}_3\text{O}_{10-\delta}$ (Ln = La, Pr, Nd, Sm, Eu, Gd) for active cathodes of low temperature solid oxide fuel cells

Journal:	<i>Journal of Materials Chemistry A</i>
Manuscript ID:	TA-ART-02-2015-001273.R1
Article Type:	Paper
Date Submitted by the Author:	14-Apr-2015
Complete List of Authors:	Chaianansutcharit, Soamwadee; Chulalongkorn University, Chemistry Hosoi, Kei; Kyushu University, Applied Chemistry Hyodo, Junji; Kyushu univ., Ju, Young-wan; Kyushu University, Applied Chemistry Ishihara, Tatsumi; Kyushu University, Department of Applied chemistry Faculty of Engineering



ARTICLE

Ruddlesden Popper oxide of $\text{LnSr}_3\text{Fe}_3\text{O}_{10-\delta}$ (Ln = La, Pr, Nd, Sm, Eu, Gd) for active cathodes of low temperature solid oxide fuel cells

S. Chaianansutcharit,^{a,c} K. Hosoi,^a J. Hyodo,^a Y.-W. Ju^{a†} and T. Ishihara^{*a,b}

Received 00th January 20xx,
Accepted 00th January 20xx

DOI: 10.1039/x0xx00000x

www.rsc.org/

Ruddlesden popper type oxide of $\text{LnSr}_3\text{Fe}_3\text{O}_{10-\delta}$ (Ln=La, Pr, Nd, Sm, Eu, Gd) has been investigated as active cathode for solid oxide fuel cells (SOFCs). Among the examined $\text{LnSr}_3\text{Fe}_3\text{O}_{10-\delta}$, it was found that $\text{PrSr}_3\text{Fe}_3\text{O}_{10-\delta}$ shows the highest activity to cathode reaction. The prepared $\text{LnSr}_3\text{Fe}_3\text{O}_{10-\delta}$ have tetragonal crystal structure with the space group $I4/mmm$. With decreasing the ionic size of Ln^{3+} , the unit cell volume and crystallite size decrease. The temperature and P_{O_2} dependence of electrical conductivities indicate the metallic-like behaviour and the predominant hole conduction. The thermal expansion coefficient (TEC) values derived from the non-linear expansion curves of $\text{LnSr}_3\text{Fe}_3\text{O}_{10-\delta}$ are reasonably compatible with those of $\text{La}_{0.9}\text{Sr}_{0.1}\text{Ga}_{0.8}\text{Mg}_{0.2}\text{O}_3$ (LSGM) electrolyte. The catalytic activity as cathode for H_2 -SOFC depended upon Ln ions. The high cathodic activity was achieved on $\text{PrSr}_3\text{Fe}_3\text{O}_{10-\delta}$ (PSFO10) and the maximum power density of 0.51 W.cm^{-2} was achieved at 1073 K when 0.3 mm thickness LSGM electrolyte was used. The surface exchange coefficient, k , also confirms the high activity for the dissociation of oxygen in PSFO10. Therefore, $\text{PrSr}_3\text{Fe}_3\text{O}_{10-\delta}$ is highly promising as cathode for low temperature SOFCs.

Introduction

Solid oxide fuel cell (SOFC) is extensively studied as a power generator with high efficiency for a decade. The compatibility of materials and the long start-up time have been recognized as major drawbacks for operation at high temperature. By lowering the operating temperature to the intermediate temperature of 773–873K, the power density of the cell is decreased due to many plausible reasons e.g. decreased oxide ion conductivity in electrolyte, large electrode overpotential, etc. Recently, the development of new cathode materials with mixed electronic and ionic conductivity (MEIC) has been considered to promote the oxygen migration at intermediate temperature^{1–6}. Layered perovskites, e.g. La_2NiO_4 ^{6,7}, $\text{Sr}_{3-x}\text{La}_x\text{Fe}_{2-y}\text{Co}_y\text{O}_7$ ($0.3 \leq x \leq 0.6$, $0 \leq y \leq 1.5$)^{8,9} have received many attention owing to the excess oxygen in the structure which contributes to the oxide ion conductivity. However, few works have been reported on electrode performance of Ruddlesden-Popper (RP) series $\text{A}_{n+1}\text{BnO}_{3n+1}$ (A= lanthanide or alkaline earth, B= transition metal, and n = the number of the layers of

octahedral in the perovskite-like stacks, e.g. $1,2,3,\dots,\infty$) with high number of octahedral layers e.g. $\text{La}_4\text{Ni}_3\text{O}_{10}$ ^{10–11}, $\text{LaSr}_3\text{Fe}_3\text{O}_{10-\delta}$ ^{9–12} because the stability of materials decreases when the number of octahedral layer increases¹³.

For triple layer-iron RP oxides, $\text{Sr}_4\text{Fe}_3\text{O}_{10-\delta}$, the thermodynamic stability can be improved by substitution of rare earth metals for Sr site¹⁴. $\text{LaSr}_3\text{Fe}_3\text{O}_{10-\delta}$ (LSFO10) has been reported to be a good candidate for SOFC cathode and oxygen separation membrane because it exhibits high conductivity, excess oxygen at room temperature, and significant amount of oxygen vacancies at high temperature around 1173 K^{9,15–17}. Recently, high oxygen reduction reaction (ORR) activity of LSFO10 is reported for air electrode of Zn-air battery¹⁸. Additionally, by substitution of Co for Fe, the conductivity and oxygen permeation flux of $\text{LaSr}_3\text{Fe}_{3-y}\text{Co}_y\text{O}_{10-\delta}$ ($0 \leq y \leq 1.5$) is drastically improved with the Co content^{8,12,17}. Therefore, the maximum power density can be achieved from 0.25 to 0.75 W.cm^{-2} depending on the type and the thickness of electrolyte^{8,9,12}. Even though $\text{LaSr}_3\text{Fe}_3\text{O}_{10-\delta}$ has studied, a few works have been done on SOFC performance of other lanthanide elements^{19,20} and there is no report of Pr, Sm, and Eu with $\text{La}_{0.9}\text{Sr}_{0.1}\text{Ga}_{0.8}\text{Mg}_{0.2}\text{O}_3$ (LSGM) electrolyte. However, because of structural similarities and thermal expansion between RP cathode and LSGM perovskite electrolyte, we reported the high potential of $\text{LnSr}_3\text{Fe}_3\text{O}_{10-\delta}$ (Ln=La, Pr, Nd, Sm, Eu, Gd) as cathode for IT-SOFC in this study. The influence of Ln^{3+} ions and aliovalence number of Ln ions on crystal structure, thermal property, oxygen exchange behavior, and electrochemical property as H_2 -fuel single cell were investigated.

^a Department of Applied Chemistry, Faculty of Engineering, Kyushu University, 744 Motoooka, Nishi-ku, Fukuoka, 819-0395, Japan. Fax: +81-92-802-2686; Tel: +81-92-802-2868. E-mail: ishihara@cstf.kyushu-u.ac.jp

^b International Institute for Carbon Neutral Energy Research (WPI-I2CNER), Kyushu University 744 Motoooka, Nishi-ku, Fukuoka, 819-0395, Japan. E-mail: ishihara@cstf.kyushu-u.ac.jp

^c Department of Chemistry, Faculty of Science, Chulalongkorn University, Bangkok 10330 Thailand. Fax: +66-2254-1309; Tel: +66-2218-7596-7. E-mail: soamwadee.c@chula.ac.th Address here.

[†] Current address: School of Energy and Chemical Engineering, Ulsan National Institute of Technology, UNIST gil 50, Banyeon-ri, Eonyang-eup, Ulsan, 689-805, Korea. Tel: +82-52-217-2935.

Experimental

Triple layer RP oxides and electrolyte were synthesized by conventional solid state reaction. Briefly discussed as follows, triple layer oxide materials, $\text{LnSr}_3\text{Fe}_3\text{O}_{10-\delta}$ (Ln=La, Pr, Nd, Sm, Eu, Gd) were prepared by grinding stoichiometric amount of starting materials e.g. La_2O_3 (Chameleon Reagent, 99.99%), Pr_6O_{11} (Soekawa Chemicals Co., 99.9%), Nd_2O_3 (Wako Co., 99.9%), Sm_2O_3 (Kishida Chemical Co., 99.9%), Eu_2O_3 (Kishida Chemicals Co., 99.99%), Gd_2O_3 (Kojundo Chemical Laboratory Co., 99.9%), SrCO_3 (Rare Metallic Co. Ltd, 99.99%), and $\alpha\text{-Fe}_2\text{O}_3$ (Wako, 99.9%) in an alumina mortar, calcining at 1273 K for 12 h in air, and firing at 1673 K for 12h. The powder was reheated at 1173 K for 30 min and cooled down to room temperature with a cooling rate of $2\text{ K}\cdot\text{min}^{-1}$ to maximize the oxygen content¹⁷. The $\text{La}_{0.9}\text{Sr}_{0.1}\text{Ga}_{0.8}\text{Mg}_{0.2}\text{O}_3$ (LSGM) electrolyte was synthesized by grinding a mixture of La_2O_3 , SrCO_3 , Ga_2O_3 (Wako, 99.99%), and MgO (Wako, 99.9%) for 30 min, calcining in air at 1273 K for 6 h, pelletizing under iso-static pressure of 300 MPa for 30 min, and sintering at 1773 K for 5 h²¹. The NiO- Fe_2O_3 (Ni:Fe ratio of 9:1) anode was prepared by modified impregnation method. $\text{FeNO}_3\cdot 9\text{H}_2\text{O}$ and NiO were dissolved in distilled water and evaporated to dryness. The oxide powder was fired at 673 K for 2 h to remove NO_x and then calcined in air at 1473 K for 6 h.

Crystal structure of the prepared sample was analyzed by using a Rigaku Rint-2500 X-ray powder diffractometer equipped with Cu $K\alpha$ radiation and a monochromator. The electrical conductivity was measured as a function of temperature (773-1173 K) and oxygen partial pressure ($P_{\text{O}_2} = 10^{-4}$ -1 atm) by a 4-probe DC method with Pt electrode. Thermal expansion coefficient (TEC) was measured in air by a Thermal Plus TMA 8310 (Rigaku) using Al_2O_3 as a reference in the temperature range of 313-1273 K and a heating rate of $10\text{ K}\cdot\text{min}^{-1}$. X-ray photoelectron spectrometry measurement was carried out with ESCA-3400 (Shimadzu, Japan) electron spectrometer equipped with Mg $K\alpha$ radiation at pressure below 10^{-5} Pa. The spectra were recorded in cycles at binding energy range of 920-980 eV after the sputtering process with Ar^+ ion beam (2 keV) for 5 min. The obtained spectrum was calibrated by assigning the binding energy of C 1s to 285 eV. SEM observation of the cells after the power generation measurement was performed by using a scanning electron microscopy (SEM, VE-7800, Keyence).

Power generation property of the fuel cell which uses triple layer RP oxides for cathode was evaluated by electrolyte-supported single cell (0.3 mm in thickness). $\text{LnSr}_3\text{Fe}_3\text{O}_{10-\delta}$ cathode and Ni-Fe anode were applied as slurry on the each surface of LSGM electrolyte by a screen-printing technique based on ethyl cellulose and an organic binder as vehicles. A Pt-wire reference was attached to the electrolyte on the cathode side using small amount of Pt paste. The single cell was then fired at 1173 K for 30 min and Pt meshes as current collectors were attached to each electrode with the effective electrode area of 0.12 cm^2 . The cell was performed at 1073, 973, and 873 K under the flow rates of $100\text{ cm}^3\cdot\text{min}^{-1}$ of O_2 and humidified H_2 ($\sim 3\%$ H_2O at 298 K) as an oxidant and a fuel,

respectively. Prior to the cell measurement, Ni-Fe anode was reduced to the metallic state at 1073 K for 1 h under the humidified H_2 flow ($100\text{ cm}^3\cdot\text{min}^{-1}$). The power density was evaluated by applying the current across the cell using a potentiostat/galvanostat (Hokuto Denko, HA-305) and measuring the potentials using a digital multimeter (Advantest, R6451A). The internal resistance of the cell was measured via a current interrupt method using a current pulse generator (Hokuto Denko, HC-111) and a Memory Hicorder (Hioki, 8835). The impedance measurement was also recorded on a frequency response analyzer (Solartron, 1255B) equipped with an electrochemical interface (Solartron, SI 1287).

Oxygen exchange rate was analyzed based on gas phase $^{16}\text{O}_2$ - $^{18}\text{O}_2$ exchange. Because the dense pellets of $\text{LnSr}_3\text{Fe}_3\text{O}_{10-\delta}$ cannot be obtained, the powder samples were used for the estimation of oxygen exchange coefficient value. The changes of isotopic fraction of ^{18}O in gas phase were analyzed with duration time at 1073 K with quadrupole mass spectroscopy and an oxygen partial pressure of 200 mbar. Isotopic exchange rate constant, k values were estimated according to Equation 1.

$$\ln\left(\frac{[^{18}\text{O}]_0 - [^{18}\text{O}]_{bg}}{[^{18}\text{O}]_t - [^{18}\text{O}]_{bg}}\right) = -kt\left(\frac{1}{n_g} + \frac{1}{n_s}\right) \quad (1)$$

where $[^{18}\text{O}]_0$ and $[^{18}\text{O}]_t$ are isotopic fraction of ^{18}O in gas phase at initial time and time t , $[^{18}\text{O}]_{bg}$ is natural isotopic background in equilibrium with gas and solid, n_s and n_g are the number of O atom in solid phase and gas phase, respectively, and t is the exchanging time. The measurement details have been reported elsewhere²². As another method for the estimation of k value, oxygen isotope exchange technique of the dense LSGM coated with $\text{LnSr}_3\text{Fe}_3\text{O}_{10-\delta}$ (Ln = La or Pr) surface coating layer was conducted. The grinded powder samples were painted on the surface of LSGM pellets by hand-printing method, and heated in normal oxygen at a pressure of 200 mbar. After annealing samples for over 16 h, the samples were quenched. After removing the normal oxygen by evacuation, 200-mbar ^{18}O was introduced at room temperature. Then the samples were heated rapidly, maintained at 1067 K for 10 min, and cooled down rapidly. The exchanged disk was cut into bar shape, and the cross sections of bar samples were polished. The ^{18}O fractions in LSGM pellets at the cross-section were analyzed by an ATOMIKA-4100 Secondary Ion Mass Spectrometer (SIMS) with line scan analysis (12.5 kV Cs^+ ion beam, spot size: ca. $30\ \mu\text{m}$). The surface concentration of oxygen isotope was measured with the depth profiling analysis with 5 keV Cs^+ beam for reducing an error of line scan analysis which is originated from the spot size of ion beam. Obtained depth profiles of ^{18}O were fitted to the diffusion equation, and oxygen self-diffusivity of LSGM (D^*) and oxygen surface exchange coefficients of LSGM with $\text{LnSr}_3\text{Fe}_3\text{O}_{10-\delta}$ (Ln = La or Pr) were estimated²³⁻²⁴.

Results and discussion

Effect of Ln ion on crystal structure and electrical conductivity

XRD patterns of $\text{LnSr}_3\text{Fe}_3\text{O}_{10-\delta}$ (Ln=La, Pr, Nd, Sm, Eu, Gd) are shown in Figure 1. The main diffraction peaks of all samples were refined based on tetragonal crystal structure with space group $I4/mmm$ of $\text{LaSr}_3\text{Fe}_3\text{O}_{9.9}$ phase (JCPDS No. 81-1234)¹⁶⁻¹⁷. The small diffraction peaks of LnBO_3 e.g. $(\text{La}_{0.3}\text{Sr}_{0.7})\text{FeO}_3$ (JCPDS No. 82-1964), and $(\text{LnA})\text{BO}_4$ e.g. SrLaFeO_4 (JCPDS No. 71-1745) were also observed as trace impurities in the samples. Apparently major phase is $\text{LnSr}_3\text{Fe}_3\text{O}_{9.9}$ obtained in this study. The main diffraction peaks are slightly shifted to a higher two theta angles when Ln ion is changed from La to Gd, suggesting a decrease in unit cell parameter and the shrinkage of unit cell volume due to decrease in the ionic size of Ln^{3+} ions. Unlike others, Sm and Eu have oxidation state of +2/+3, which results in a long A-O bond causing a lower shift in the diffraction angle from (017) and (110), and the expansion of unit cell volume from Nd to Sm and Eu. The unit cell parameter calculated from the diffraction peaks of (017) and (110) planes and the crystallite size of materials calculated from the (017) peak using Scherrer equation are summarized in Table 1. With decreasing the ionic size of Ln ion, the bond length between Ln-O decreases resulting in the contraction of unit cell along a - or c -axis and a decreasing trend of crystallite size. Even though the crystallite sizes of $\text{LnSr}_3\text{Fe}_3\text{O}_{10-\delta}$ materials are varied, no significant differences in particle size are observed as displayed in Figure 2. The particle sizes of materials were analyzed using the particle size analyzer mainly in the range of 1-2 μm .

Thermal expansion properties of $\text{LnSr}_3\text{Fe}_3\text{O}_{10-\delta}$ (Ln=La, Pr, Nd, Sm, Eu, Gd) were measured in air at 353-1273 K. All

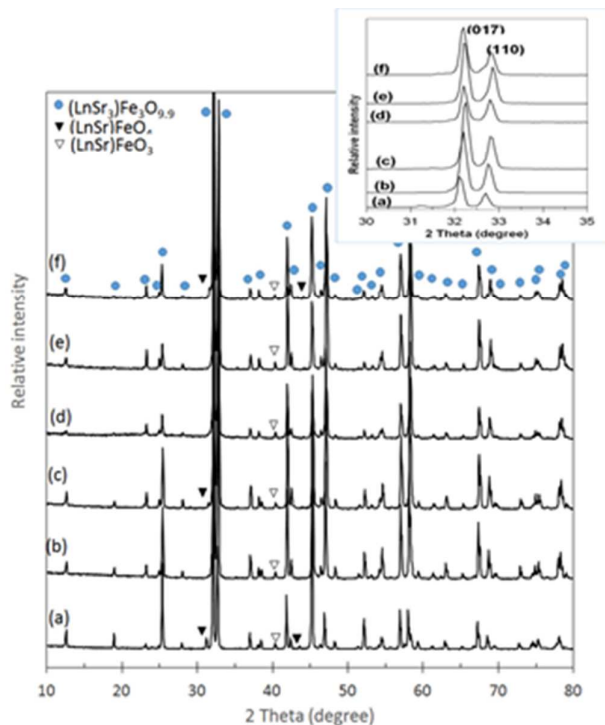


Figure 1 XRD patterns of $\text{LnSr}_3\text{Fe}_3\text{O}_{10-\delta}$ (Ln=La, Pr, Nd, Sm, Eu, Gd) (a) $\text{LaSr}_3\text{Fe}_3\text{O}_{10-\delta}$, (b) $\text{PrSr}_3\text{Fe}_3\text{O}_{10-\delta}$, (c) $\text{NdSr}_3\text{Fe}_3\text{O}_{10-\delta}$, (d) $\text{SmSr}_3\text{Fe}_3\text{O}_{10-\delta}$, (e) $\text{EuSr}_3\text{Fe}_3\text{O}_{10-\delta}$, and (f) $\text{GdSr}_3\text{Fe}_3\text{O}_{10-\delta}$.

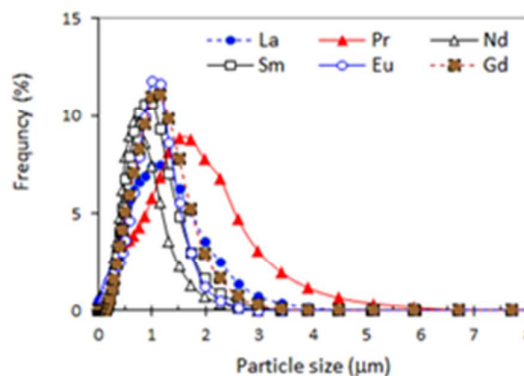


Figure 2 Particle size distribution of $\text{LnSr}_3\text{Fe}_3\text{O}_{10-\delta}$ (Ln=La, Pr, Nd, Sm, Eu, Gd).

samples exhibit a linear thermal expansion behavior at temperature below 573 K due to the negligible oxygen loss⁸ but at high temperature, thermal expansion non-linearly increased as shown in Figure 3. At high temperature, increase in bond energy causes the increase in bond lengths of Ln-O and B-O bonds in the structure. As a result, oxygen loss increases and the materials are easily expanded. With decreasing the ionic size of Ln^{3+} ion from La to Nd and Gd, the thermal expansion coefficient (TEC) tends to decrease as shown in Table 1 because a strong bond is formed by shortening Ln-O bond length. This decreasing trend is also in agreement with the effect of Ln^{3+} in $n = 2$ member of RP series²⁵, $\text{Sr}_{2.7}\text{Ln}_{0.3}\text{Fe}_{1.4}\text{Co}_{0.6}\text{O}_{7-\delta}$. For $\text{PrSr}_3\text{Fe}_3\text{O}_{10-\delta}$, Pr has oxidation number of +3/+4 but the TEC value is quite high compared to others. It could be contributed to large amount of oxygen vacancies. With increasing oxygen vacancies, the electrostatic attraction of B-O bond reduces by charge compensation of Fe, a reduction of Fe^{4+} to Fe^{3+} , causing the increase in TEC value¹². However, comparing with that of LSGM electrolyte ($11.6 \times 10^{-6} \text{ K}^{-1}$), TEC of $\text{LnSr}_3\text{Fe}_3\text{O}_{10-\delta}$ is in the similar value, in particular, at temperature range of 353-800 K,

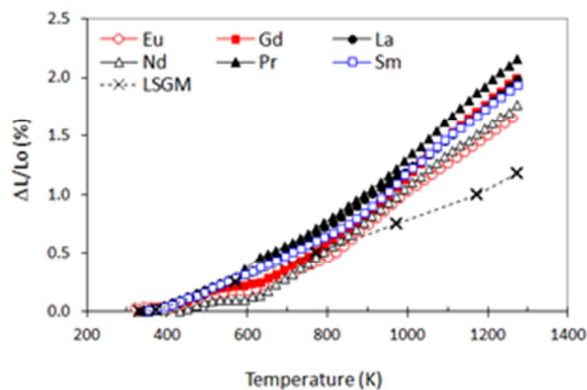


Figure 3 Thermal expansion curves of $\text{LnSr}_3\text{Fe}_3\text{O}_{10-\delta}$ (Ln=La, Pr, Nd, Sm, Eu, Gd) as a function of temperature.

Table 1 Structural property and thermal expansion coefficient of $\text{LnSr}_3\text{Fe}_3\text{O}_{10-\delta}$ (Ln=La, Pr, Nd, Sm, Eu, Gd)

Materials	Ionic radii, Ln^{3+} (\AA)*	Unit cell parameter (\AA)		V (\AA^3)	Crystallite size (nm)	$\text{TEC} \times 10^{-6}$ (K^{-1})		E_a (eV)
		a	c			353-773 K	353-1073 K	
$\text{LaSr}_3\text{Fe}_3\text{O}_{10-\delta}$	1.36	3.868	28.016	419.190	57	14.4	17.5	1.36
$\text{PrSr}_3\text{Fe}_3\text{O}_{10-\delta}$	1.179	3.859	27.994	416.851	50	16.7	21.3	1.22
$\text{NdSr}_3\text{Fe}_3\text{O}_{10-\delta}$	1.27	3.857	27.944	415.644	48	11.0	17.5	1.21
$\text{SmSr}_3\text{Fe}_3\text{O}_{10-\delta}$	1.24	3.858	28.002	416.752	48	14.4	19.4	1.11
$\text{EuSr}_3\text{Fe}_3\text{O}_{10-\delta}$	1.12	3.852	28.033	415.838	47	8.9	16.1	1.17
$\text{GdSr}_3\text{Fe}_3\text{O}_{10-\delta}$	1.107	3.857	28.031	416.965	45	12.0	23.5	1.28

*Shannon ionic radii (1976), coordination number of 12

however, slightly larger above 800 K. Although the some differences in TEC of $\text{LnSr}_3\text{Fe}_3\text{O}_{10-\delta}$ against that of LSGM are observed at temperature higher than 800 K, there is no delamination of electrode excepting for $\text{NdSr}_3\text{Fe}_3\text{O}_{10-\delta}$. As discussed later, some of Fe was diffused from cathode to electrolyte. Therefore, it is expected that Fe composition is gradient at electrolyte and cathode interface. As a result, delamination of cathode from LSGM electrolyte may not be observed. On the other hand, small change in slope of TEC was observed around 673 and 1273K, phase change of RP phase which may related with thermal reduction of Fe or Co is suspected and this seems to be main reason for low sintering property.

Figure 4 shows the temperature and P_{O_2} dependences of electrical conductivity of $\text{LnSr}_3\text{Fe}_3\text{O}_{10-\delta}$ (Ln=La, Pr, Nd, Sm, Eu, Gd). The conductivity decreases with increasing temperature from 673 to 1273 K suggesting metallic-like behaviour. For the

P_{O_2} dependence of electrical conductivity in Figure 4(b), the conductivities of $\text{LnSr}_3\text{Fe}_3\text{O}_{10-\delta}$ decreased with decreasing oxygen partial pressure suggesting the dominant hole conduction in these $\text{LnSr}_3\text{Fe}_3\text{O}_{10-\delta}$, however, it is considered that reduction may be occurred at lower P_{O_2} range because of high oxidation number of Fe. The conductivities of $\text{LnSr}_3\text{Fe}_3\text{O}_{10-\delta}$ were strongly dependent on Ln ions. The large ionic size of Ln tends to have higher electrical conductivity than that of the smaller one, which may be related to the distortion of crystal structure by decrease in ionic size from La to Gd. Then mobility of electrons seems to be decreased. In addition to the ionic size of A, changing in oxidation number of A also affect the oxidation number of Fe in B site, which relates to the number of oxygen vacancy or ionic conductivity¹². Therefore the mobility as well as number of hole may be changed with ionic size of Ln. In this study, $\text{PrSr}_3\text{Fe}_3\text{O}_{10-\delta}$ shows the highest conductivity value compared to others and this may be

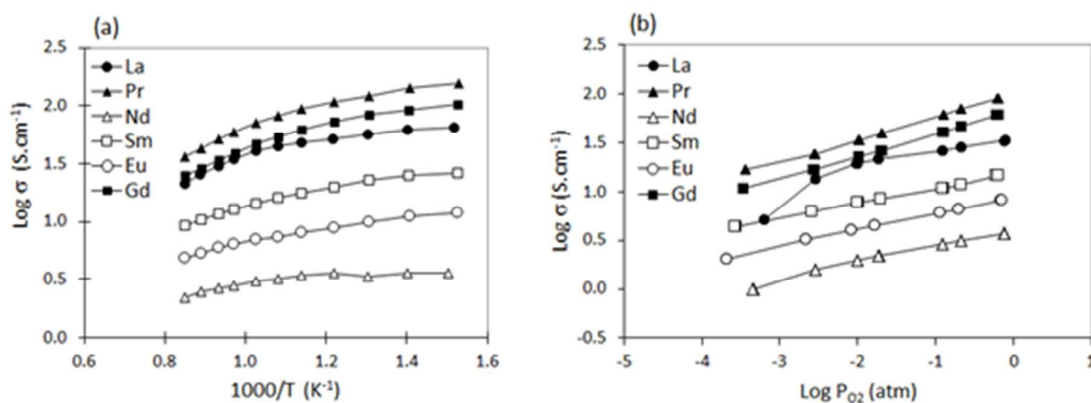
Figure 4 Temperature dependence (a) and P_{O_2} dependence (b) of electrical conductivity of $\text{LnSr}_3\text{Fe}_3\text{O}_{10-\delta}$ (Ln=La, Pr, Nd, Sm, Eu, Gd).

Table 2 Electrochemical performance of $\text{LnSr}_3\text{Fe}_3\text{O}_{10-\delta}$ | LSGM | Ni-Fe (Ln=La, Pr, Nd, Sm, Eu, Gd)

Cathode	1073 K			973 K			873 K		
	MPD (mW.cm^{-2})	IR_{loss} (mV)	η_c (mV)	MPD (mW.cm^{-2})	IR_{loss} (mV)	η_c (mV)	MPD (mW.cm^{-2})	IR_{loss} (mV)	η_c (mV)
$\text{La}_{0.6}\text{Sr}_{0.4}\text{Fe}_{0.8}\text{Co}_{0.2}\text{O}_3$	443	294	113	110	272	69	17	103 ^[b]	16 ^[b]
$\text{LaSr}_3\text{Fe}_3\text{O}_{10-\delta}$	464	237	59	172	121	87	50	62	68
$\text{PrSr}_3\text{Fe}_3\text{O}_{10-\delta}$	514	168	65	337	109	62	48	59	46
$\text{NdSr}_3\text{Fe}_3\text{O}_{10-\delta}$	258	440	84	86	394	109	27	212	103
$\text{SmSr}_3\text{Fe}_3\text{O}_{10-\delta}$	383	287	56	101	262	75	31	159	59
$\text{EuSr}_3\text{Fe}_3\text{O}_{10-\delta}$	429	243	81	145	193	90	33	128	81
$\text{GdSr}_3\text{Fe}_3\text{O}_{10-\delta}$	356	278	78	116	156 ^[a]	87 ^[a]	29	146	93

The cell performance at 1073, 973 and 873 K was recorded at current density of 500, 150 and 50 mA.cm^{-2} , respectively. ^[a] At current density of 125 mA.cm^{-2} . ^[b] At current density of 30 mA.cm^{-2} .

attributed to the mixed oxidation state of Pr as +3 and +4 which promotes the formation of hole. On the contrary, $\text{NdSr}_3\text{Fe}_3\text{O}_{10-\delta}$ (NSFO10) shows the lowest conductivity even though it has the oxidation number of +3 similar to Gd. This data is in contrast with the conductivity reported by Kim et al.¹⁹, who reported the conductivity of Nd is higher than that of Gd. A plausible reason may be attributed to the phase impurity and phase stability of NSFO10 prepared in this work. It is also noted that electrical conductivity of Pr_2NiO_4 and La_2NiO_4 are reported as 125 and 89 Scm^{-1} at 973 K, respectively, in air.²⁶ Therefore, the electrical conductivity of $\text{LnSr}_3\text{Fe}_3\text{O}_{10-\delta}$ is similarly high with that of Ln_2NiO_4 which is reported as active cathode.²⁶

Cathodic performance of $\text{LnSr}_3\text{Fe}_3\text{O}_{10-\delta}$

The cathodic performance of $\text{LnSr}_3\text{Fe}_3\text{O}_{10-\delta}$ (Ln = La, Pr, Nd, Sm, Eu, Gd), was evaluated by using the cell where 0.3 mm thick LSGM and Ni-Fe were used for electrolyte and anode, respectively. Maximum power density (MPD), cathodic IR loss (IR_{loss}) and cathodic overpotential (η_c) are summarized in Table 2 and the polarization as a function of current density is shown in Figure 5. The cell performance using LSCF cathode which is widely used cathode was also shown in Table 2 for comparison. Obviously, compared with the power density of the cell using $\text{La}_{0.6}\text{Sr}_{0.4}\text{Fe}_{0.8}\text{Co}_{0.2}\text{O}_3$ (LSCF) cathode, all cells using $\text{LnSr}_3\text{Fe}_3\text{O}_{10-\delta}$ for cathode shows reasonably high power density in the range of 300-500 mW.cm^{-2} . Cathodic overpotential was smaller than 100 mV at 1073 K, indicating all $\text{LnSr}_3\text{Fe}_3\text{O}_{10-\delta}$ have good surface activity for oxygen dissociation. With decreasing the operating temperature, the

power densities decrease because of increased IR loss and decreased cathodic activity, however, comparing with the IR loss and overpotential of the cell using LSCF cathode, decrease in power density is still not large. One reason for high surface activity to oxygen dissociation is assigned to the large amount of oxygen vacancy and also its high mobility in this oxygen deficient RP structure¹⁴. The maximum power density of the cell using $\text{LnSr}_3\text{Fe}_3\text{O}_{10-\delta}$ cathode was changed by the Ln ions.

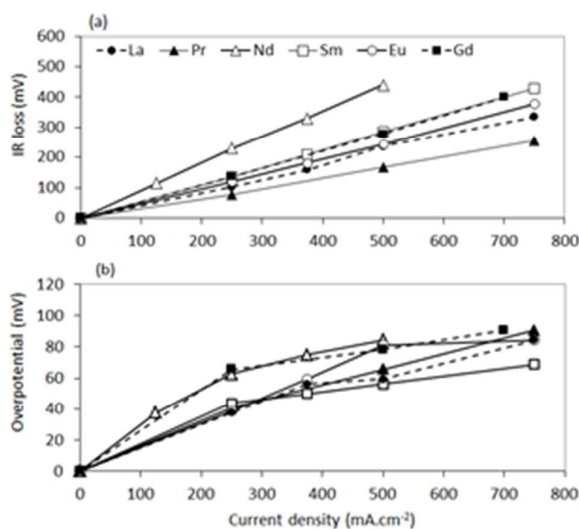


Figure 5 Polarization of $\text{LnSr}_3\text{Fe}_3\text{O}_{10-\delta}$ (Ln=La, Pr, Nd, Sm, Eu, Gd) as a function of current density at 1073 K, (a) cathodic IR loss, (b) cathodic overpotential.

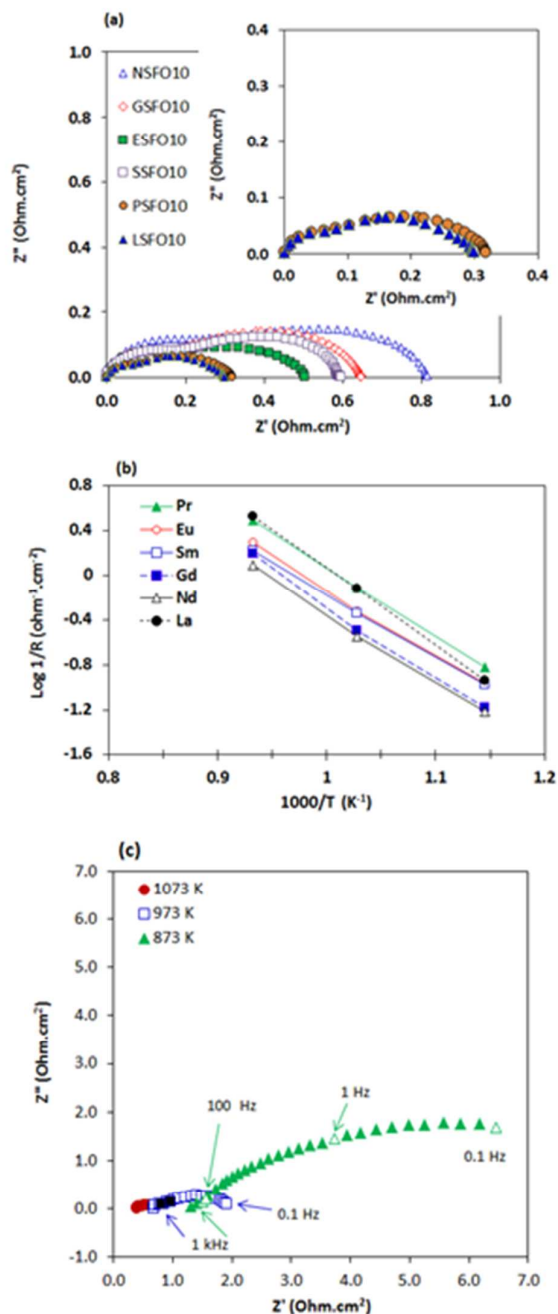


Figure 6 Comparative cathodic impedance plots for cells of LnSr₃Fe₃O_{10-δ} (Ln=La, Pr, Nd, Sm, Eu, Gd) cathodes on LSGM electrolyte at 1073 K, (b) The Arrhenius plot of polarization resistance of LnSr₃Fe₃O_{10-δ} cathodes, and (c) Typical cathodic impedance plots of PrSr₃Fe₃O_{10-δ} cathode.

For Ln³⁺ ions, the power densities increased in the following order at 1073 K, Pr > La > Eu > Sm > Gd > Nd which almost corresponds to the lower values of IR_{loss}. Even though the conductivity of GdSr₃Fe₃O_{10-δ} is slightly higher than that of LaSr₃Fe₃O_{10-δ}, decrease in power density was more significant

and this was explained by large ASR value of GdSr₃Fe₃O_{10-δ}, which may be assigned to the contact resistance. When the contact between cathode and electrolyte is poor, the IR_{loss} became large but polarization of electrode also became larger. Therefore, one reason for large ASR of GdSr₃Fe₃O_{10-δ} may be assigned to the poor contact to LSGM electrolyte because TEC of GdSr₃Fe₃O_{10-δ} shows large bending around 873K (Figure 3). In fact, GaSr₃Fe₃O_{10-δ} electrode was detached during removing the cell from measurement set-up. Consequently, LaSr₃Fe₃O_{10-δ} or PrSr₃Fe₃O_{10-δ} exhibited the small IR loss and cathodic overpotential which represents the large number of active sites. This result is also in good agreement with SOFC performance reported by Kim et al.¹⁹

Reasonably large power density of EuSr₃Fe₃O_{10-δ} seems to be assigned to the small cathodic overpotential and this could be explained by the large amount of oxygen vacancy or higher oxidation number of Fe considering the mixed valence of Eu^{3+/2+}. At high temperature, LaSr₃Fe₃O_{10-δ} loses its lattice oxygen and forms oxygen vacancy; thus the charge-neutrality is compensated with the reduction of Fe⁴⁺ to Fe³⁺.¹⁶ In case of EuSr₃Fe₃O_{10-δ}, the average valence number of iron increases comparing to LaSr₃Fe₃O_{10-δ}, and small cathodic overpotential could be explained by larger amount of active site resulting from mixed valence of Fe and Eu. On the contrary, PrSr₃Fe₃O_{10-δ} has the average valence number of iron lower than that of LaSr₃Fe₃O_{10-δ} because of higher average number of Pr³⁺, thus the increase in oxygen content of PrSr₃Fe₃O_{10-δ} accelerates the hole conductivity, and so lower IR loss on PrSr₃Fe₃O_{10-δ} can be assigned to the high hole conductivity. However, the cathodic overpotential of PrSr₃Fe₃O_{10-δ} is slightly larger than that of LaSr₃Fe₃O_{10-δ} at 1073 K, and this may relate with decreased amount of oxygen vacancy in PrSr₃Fe₃O_{10-δ}. In any way, it is seen that PrSr₃Fe₃O_{10-δ} shows the highest power density among LnSr₃Fe₃O_{10-δ} series cathode studied because of small IR_{loss}.

Figure 6 (a) shows the complex impedance plots of LnSr₃Fe₃O_{10-δ} cathode. Obviously, there are several semicircles observed, roughly two semicircles. The impedance semicircle at higher frequency could be assigned to the surface activity to oxygen dissociation and the second one at lower frequency is the diffusion overpotential. Although the particle size distribution is almost the same among LnSr₃Fe₃O_{10-δ} as discussed, diffusion overpotential was significantly varied depending on the Ln ion in LnSr₃Fe₃O_{10-δ}. Therefore, this difference could be assigned to the difference in effective electrode area, which may be related with oxide ion conductivity in LnSr₃Fe₃O_{10-δ}.

Area specific resistance (ASR) of the cells for LnSr₃Fe₃O_{10-δ} (Ln=La, Pr, Nd, Sm, Eu, Gd) cathode with LSGM electrolyte was estimated. The polarization resistance (R_p) estimated from the high frequency and low frequency intersections as a function of temperature are plotted in Figure 6 (b). The cathodic polarization resistances of materials decrease with increasing temperature suggesting the increased activity at high temperature. LaSr₃Fe₃O_{10-δ} (LSFO10) and PrSr₃Fe₃O_{10-δ} (PSFO10) have lower internal resistance than that of SmSr₃Fe₃O_{10-δ} (SSFO10) and EuSr₃Fe₃O_{10-δ} (ESFO10), which is in

good agreement with the conductivity data, *i.e.* both $\text{LaSr}_3\text{Fe}_3\text{O}_{10-\delta}$ and $\text{PrSr}_3\text{Fe}_3\text{O}_{10-\delta}$ show higher conductivity than that of others. In addition, the slopes of temperature dependence are also the same suggesting the reaction mechanisms are also the same in all electrodes studied. The activation energy (E_a) of $\text{LnSr}_3\text{Fe}_3\text{O}_{10-\delta}$ was calculated based on Arrhenius equation and summarized in Table 1. No significant variation in E_a values is obviously related to ionic radii of Ln; however a decrease trend in activation energy is noticed when changing from La to other lanthanides. This may be related with oxide ion conductivity in $\text{LnSr}_3\text{Fe}_3\text{O}_{10-\delta}$, *i.e.*, active site for cathode reaction can be expanded from three phase to two phase boundary with increasing oxide ion conductivity in cathode. In case of $\text{NdSr}_3\text{Fe}_3\text{O}_{10-\delta}$, the E_a value is quite reasonable in $\text{LnSr}_3\text{Fe}_3\text{O}_{10-\delta}$ but the ASR value is very high, suggesting the stability of $\text{NdSr}_3\text{Fe}_3\text{O}_{10-\delta}$ seems not to be high.

Figure 6 (c) shows cathodic impedance plot of $\text{PrSr}_3\text{Fe}_3\text{O}_{10-\delta}$ at 1073, 973, and 873K. Although impedance arc was much small at 1073 K, it increased significantly with decreasing operating temperature. In particular, increase in semicircles at lower frequency is significant suggesting that diffusion overpotential became larger with decreasing temperature. However, impedance semicircle at higher frequency is kept small value suggesting that activation overpotential is still small at 873K and so $\text{PrSr}_3\text{Fe}_3\text{O}_{10-\delta}$ shows high activity to oxygen dissociation at 873K.

After the power generation measurements, the XRD measurements were performed for phase transformation or decomposition. The XRD patterns of $\text{PrSr}_3\text{Fe}_3\text{O}_{10-\delta}$ and $\text{NdSr}_3\text{Fe}_3\text{O}_{10-\delta}$ shown in Figure 7 indicated that the structures of $\text{PrSr}_3\text{Fe}_3\text{O}_{10-\delta}$ and $\text{NdSr}_3\text{Fe}_3\text{O}_{10-\delta}$ were stable and

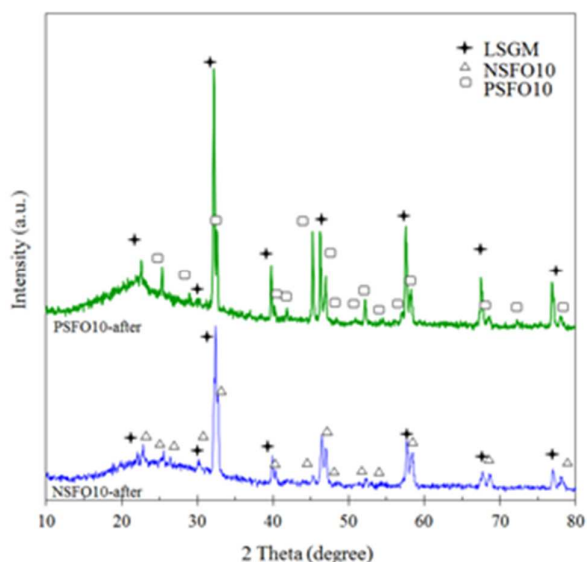


Figure 7 spectra of $\text{PrSr}_3\text{Fe}_3\text{O}_{10-\delta}$ (PSFO10) and $\text{NdSr}_3\text{Fe}_3\text{O}_{10-\delta}$ (NSFO10) after the power generation measurement

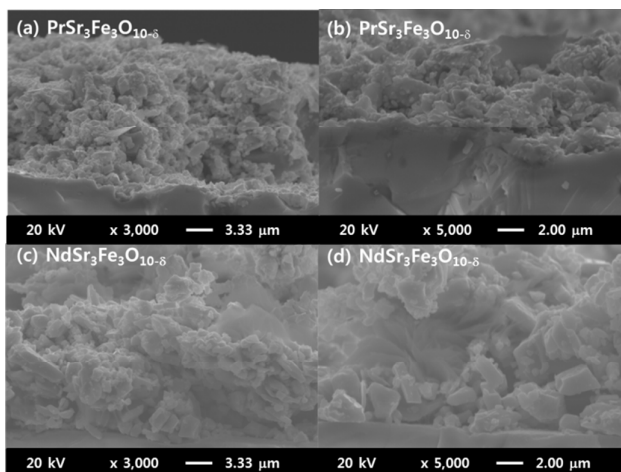


Figure 8 SEM cross section images of $\text{PrSr}_3\text{Fe}_3\text{O}_{10-\delta}$ (a-b) and $\text{NdSr}_3\text{Fe}_3\text{O}_{10-\delta}$ (c-d) after the power generation measurement

decomposition of crystal structure was hardly observed after power generation measurements. Even though the diffraction peak intensity is rather small, the main diffraction peaks of materials and LSGM can be observed. No phase transformation or phase interaction between cathodes and electrolyte is taking place. SEM images of cross-section of the cell are also shown in Figure 8. It is clearly observed that no delamination occurs along the electrode-electrolyte interface from the low magnification image. However a slightly larger in particle size of $\text{NdSr}_3\text{Fe}_3\text{O}_{10-\delta}$ can be observed from the high magnification image, suggesting an agglomeration of particles during operation, which may be related with the initial small degradation of SOFC performance of $\text{NdSr}_3\text{Fe}_3\text{O}_{10-\delta}$ used cell. This agglomeration of particles is confirmed by the particle size analysis of materials before the reaction in Figure 2 which indicates the average particle size of $\text{NdSr}_3\text{Fe}_3\text{O}_{10-\delta}$ is smaller than those of $\text{PrSr}_3\text{Fe}_3\text{O}_{10-\delta}$.

Surface activity for oxygen dissociation

The surface exchange coefficient, k , of $\text{PrSr}_3\text{Fe}_3\text{O}_{10-\delta}$ and $\text{LaSr}_3\text{Fe}_3\text{O}_{10-\delta}$ were determined by isotopic exchange of ^{18}O . For gas phase analysis of the isotopic exchange, the normalized concentration of ^{18}O as a function of exchanging time is shown in Figure 9. Tracer oxygen concentration, $[^{18}\text{O}]$ increased with reaction time, indicating the isotope exchanging reaction was monitored successfully. Surface exchange coefficient, k value can be calculated from the slope of the plots based on equation (1). The obtained k value of $\text{PrSr}_3\text{Fe}_3\text{O}_{10-\delta}$ ($5.20 \times 10^{-7} \text{ s}^{-1}$) is four times larger than that of $\text{LaSr}_3\text{Fe}_3\text{O}_{10-\delta}$ ($1.38 \times 10^{-7} \text{ s}^{-1}$), indicating the surface activity of $\text{PrSr}_3\text{Fe}_3\text{O}_{10-\delta}$ which includes the following process: adsorption of oxygen molecule, dissociation of oxygen molecule to oxide ion and a charge transfer process, and the incorporation of oxide ion into a surface vacancy. The enhancement in active surface of $\text{PrSr}_3\text{Fe}_3\text{O}_{10-\delta}$ is in good agreement with low cathodic overpotential in this study. In addition to the gas phase measurement, the isotopic exchange in solid phase analysis

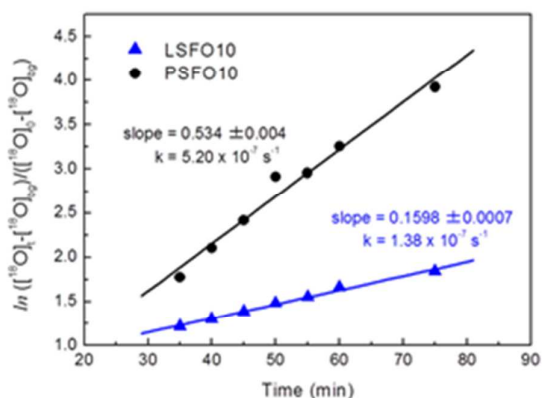


Figure 9 Time dependence of normalized isotopic fraction for $\text{PrSr}_3\text{Fe}_3\text{O}_{10-\delta}$ (PSFO10) and $\text{LaSr}_3\text{Fe}_3\text{O}_{10-\delta}$ (LSFO10). The exchange of ^{18}O was performed at 1073 K

also performed using LSGM pellets coated with PSFO10 or LSFO10. ^{18}O isotopic fraction profiles of LSGM coated with $\text{LaSr}_3\text{Fe}_3\text{O}_{10-\delta}$ and $\text{PrSr}_3\text{Fe}_3\text{O}_{10-\delta}$ are shown in Figure 10, and are compared with that of LSGM²⁷. The depth profile of normalized $[^{18}\text{O}]$ indicates the isotopic exchange efficiency of $\text{PrSr}_3\text{Fe}_3\text{O}_{10-\delta}$ is better than that of $\text{LaSr}_3\text{Fe}_3\text{O}_{10-\delta}$. By using the diffusion equation of solid reported by Crank²³, the values of D^* and k were calculated and summarized in Table 3. It is seen that k value of LSGM disc coated with PSFO10 is larger than that of LSFO10, and this tendency is the same with the results of gas-phase measurement. Theoretically, LSGM should show the same D^* values regardless of the surface coating with LSFO10 or PSFO10 powders, however, the obtained self-diffusion coefficients of LSGM with powders were slightly higher than that of LSGM as reported in our previous work²⁷. This may be due to the inter-diffusion of Fe and/or Pr into LSGM. In any way, PSFO10 exhibits higher activity to oxygen

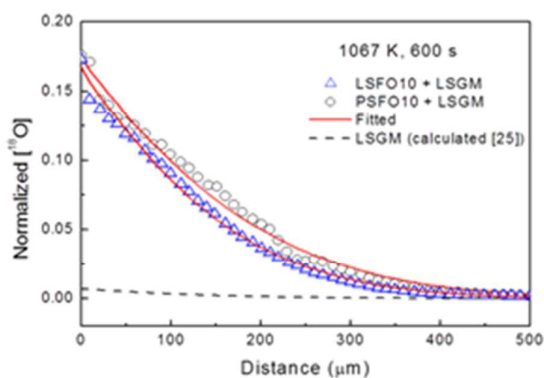


Figure 10 Depth profile of normalized isotopic oxygen fraction in only LSGM²⁷, and in LSGM coated with PSFO10 or LSFO10.

Table 3 List of D^* and k values obtained from isotopic exchange of ^{18}O in solid-phase analysis

Sample	D^* ^(a) ($\times 10^{-7} \text{ cm}^2 \text{ s}^{-1}$)	k ^(a) ($\times 10^{-6} \text{ cm s}^{-1}$)	k ^(b) ($\times 10^{-7} \text{ s}^{-1}$)
LSGM	3.24 ^[25]	0.143 ^[25]	-
LSGM+LSFO10	3.9 ± 0.1	4.40	1.38
LSGM+PSFO10	4.96 ± 0.07	5.21	5.20

^(a) The values are obtained from line-scanning technique.

^(b) The values are obtained from gas phase analysis. These values are related to only PSFO10 or LSFO10.

dissociation than that of LSFO10 and reasonably small cathodic overpotential of PSFO10 could be explained by high surface activity to oxygen dissociation. Figure 11 shows the depth

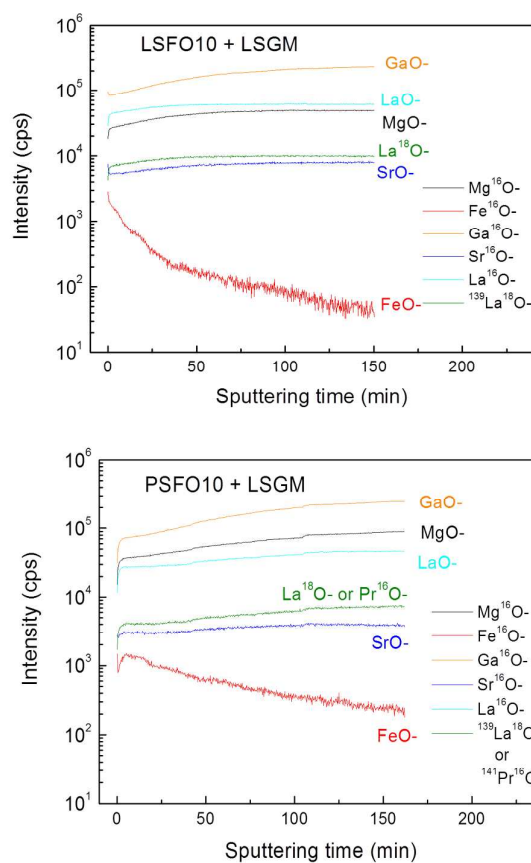


Figure 11 Depth profile of cation distribution after the isotope oxygen exchange experiments at 1067 K for 10 min; (a) LSFO10 + LSGM, (b) PSFO10 + LSGM.

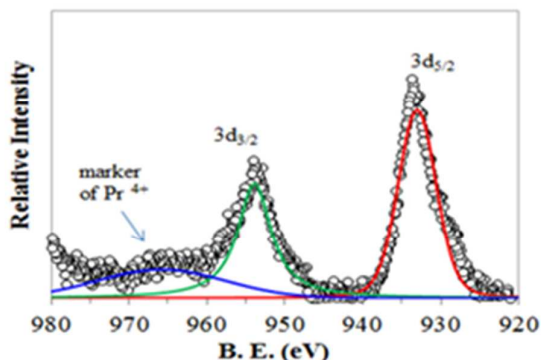


Figure 12 XPS spectra of Pr 3d of $\text{PrSr}_3\text{Fe}_3\text{O}_{10-\delta}$

profiles of cations after exchanging experiment measured by SIMS. The measurement of SIMS in Figure 11 is performed on LSGM surface after removing cathode powder. Therefore, spattering time "0" means the interface between $\text{LnSr}_3\text{Fe}_3\text{O}_{10-\delta}$ and LSGM. Obviously, Fe diffused into LSGM pellets in the both cases of LSFO10 and PSFO10. Ishihara et al. reported that the oxide ion conductivity was increased by substitution of Fe to Ga in LSGM²⁸. Therefore, the observed slightly higher self-diffusion coefficients in LSGM coated with LSFO10 or PSFO10 might be explained by the Fe diffusion in LSGM. Therefore, the observed higher D value of LSGM coated with LSFO10 or PSFO10 than that of non-coated LSGM may be explained by the diffusion of Fe from cathode to LSGM electrolyte. This suggests that at the interface between $\text{LnSr}_3\text{Fe}_3\text{O}_{10-\delta}$ and LSGM, Fe concentration is functional gradient and so more tight contact can be achieved and so, one reason for reasonably small IR loss and cathodic overpotential seems to be assigned to this tight contact of $\text{LnSr}_3\text{Fe}_3\text{O}_{10-\delta}$ to LSGM. In fact, good contact was observed by SEM. In addition, slightly increased oxide ion conductivity of LSGM by Fe diffusion is also positively work for small overpotential of cathode because oxygen can be transport from cathode to electrolyte quickly. In any case, these isotopic exchange results confirmed that PSFO10 shows the larger surface exchange coefficient k than that of LSFO10, which is main reason for small cathodic overpotential discussed above.

XPS analysis of Pr 3d in Figure 12 indicates $\text{PrSr}_3\text{Fe}_3\text{O}_{10-\delta}$ has mixed oxidation state of Pr as +3 and +4 on the surface. The binding energy at 933 and 954 eV assigned to Pr $3d_{5/2}$ and $3d_{3/2}$ can be attributed to the spectra of Pr_2O_3 whereas the $3d_{5/2}$ peak marker of Pr^{4+} , PrO_2 , is observed at binding energy of 965 eV^{29,30}. Therefore, $\text{PrSr}_3\text{Fe}_3\text{O}_{10-\delta}$ shows a high activity to oxygen dissociation because of large non-stoichiometry of oxygen comparing with other $\text{LnSr}_3\text{Fe}_3\text{O}_{10-\delta}$ (Ln=La, Nd, Sm, Eu, Gd). The high values in electrical conductivity and power density in SOFC can be explained in term of high electronic and oxide ionic conductivity.

Conclusions

The influence of Ln ions in $\text{LnSr}_3\text{Fe}_3\text{O}_{10-\delta}$ (Ln=La, Pr, Nd, Sm, Eu, Gd) on electrical conductivity as well as cathodic activity was investigated. All samples exhibit the tetragonal crystal structure with the space group of $I4/mmm$. With decreasing the ionic size of Ln^{3+} ion, the unit cell parameter, unit cell volume and crystallite size of materials decrease. The thermal expansion coefficients of $\text{LnSr}_3\text{Fe}_3\text{O}_{10-\delta}$ materials derived from the non-linear expansion curve are in the range of $16\text{--}23 \times 10^{-6} \text{ K}^{-1}$ for 373–1073 K. The temperature dependence on electrical conductivities indicates $\text{LnSr}_3\text{Fe}_3\text{O}_{10-\delta}$ has the metallic-like conducting behaviour in temperature range of 673–1273 K whereas the decreasing of conductivity under the partial pressure of O_2 of 10^{-4} –1 atm implies the *p*-type conduction in these oxide materials. The electrochemical performance based on the planar cell suggests $\text{LnSr}_3\text{Fe}_3\text{O}_{10-\delta}$ is the active cathode for SOFC; however, the catalytic activity of materials depends upon Ln ions and aliovalence number of ions, which can be explained in term of IR_{loss} , cathodic overpotential, activation energy, structural distortion and oxygen exchange behaviour. Although all materials show distinguished character of low cathodic overpotential below 100 mV, it was found that $\text{PrSr}_3\text{Fe}_3\text{O}_{10-\delta}$ shows the highest conductivity, lowest IR loss, and high activity to oxygen dissociation for SOFC cathode in this study.

Acknowledgements

Part of this work was financially supported by JSPS Grant-in-Aid for Scientific Research (S) (No. 24226016).

References

- 1 T. Ishihara, *Perovskite Oxide for Solid Oxide Fuel Cells*, Springer, 2009, pp. 302
- 2 B. An, W. Zhou, Y. Guo, R. Ran and Z. Shao, *Inter J. Hydrogen Energy*, 2010, **35**, 5601.
- 3 K. Świerczek, *Solid state Ionics*, 2011, **192**, 486.
- 4 M. Yashima, H. Yamada, S. Nuansaeng and T. Ishihara, *Chem. Mater.*, 2012, **24**, 4100.
- 5 J. Xie, Y.-W. Ju, M. Matsuka, S. Ida and T. Ishihara, *J. Power Sources*, 2013, **228**, 229.
- 6 R. J. Woolley and S. J. Skinner, *J. Power Source*, 2013, **243**, 790.
- 7 S. Choi, S. Yoo, J. Y. Shin and G. Kim, *J. Electrochem. Soc.*, 2011, **158**, 8995.
- 8 K. T. Lee, D. M. Bierschenk and A. Manthiram, *J. Electrochem. Soc.*, 2006, **153**, A1255.
- 9 C. Torres-Garibay and D. Kovar, *J. Power Sources*, 2009, **192**, 396.
- 10 G. Amow, I. J. Davidson and S. Skinner, *J. Solid State Ionics*, 2006, **177**, 1205.
- 11 G. Amow, J. Au and I. Davidson, *J. Solid State Ionics*, 2006, **177**, 1837.
- 12 K. T. Lee and A. Manthiram, *Chem Mater.*, 2006, **18**, 1621
- 13 B. V. Bennosikov and K. S. Aleksandrov, *Crystallography Reports*, 2000, **45**, 864.
- 14 J. Y. Lee, J. S. Swinnea, H. Steinfink, W. M. Reiff, S. Pei and J. D. Jorgensen, *J. Solid State Chem.*, 1993, **103**, 1.

- 15 N. Velinov, N. Brashkova and V. Kozhukharov, V. *Ceramics-Silikáty.*, 2005, **49**, 29.
- 16 G. Zhang, Q. Li, J. Cao and M. Cui, *J. Rare Earths*, 2010, **2**, 270.
- 17 T. Armstrong, F. Prado, F. and A. Manthiram, *Solid State Ionics*, 2001, **140**, 89.
- 18 T. Takeguchi, T. Yamanaka, H. Takahashi, H. Watanabe, T. Kuroki, H. Nakanishi, Y. Orikasa, Y. Uchimoto, H. Takano, N. Ohiguri, M. Matsuda, T. Murota, K. Uosaki, and W. Ueda, *J. Am. Chem. Soc.*, 2013, **135**, 11125.
- 19 J.-H. Kim, K.-T. Lee, Y. N. Kim and A. Manthiram, *J. Mater Chem.* 2011, **21**, 2482.
- 20 J.-H. Kim, Y. N. Kim, K.-T. Lee and A. Manthiram, *ECS Transaction.* 2011, **35**(1), 2137.
- 21 T. Ishihara, H. Matsuda and Y. Takita, *J. Am. Chem. Soc.*, 1994, **116**, 3801.
- 22 K. Harada, T. Oishi, S. Hamamoto and T. Ishihara, *J. Phys. Chem. C.* 2014, **118**, 559.
- 23 J. Crank, *The Mathematics of Diffusion*, Oxford University Press, 2nd edn., 1975.
- 24 R. J. Chater, S. Carter, J. A. Kilner and B. Steele, *Solid State Ionic*, 1992, **53–56**, 859.
- 25 J-H. Kim and A. Manthiram, *Solid State Ionics*, 2009, **180**, 1478.
- 26 A. V. Kovalevsky, V. V. Kharton, A. A. Yaremchenko, Y. V. Pivak, E. V. Tsipis, S. O. Yakovlev, A. A. Markov, E. N. Naumovich and J. R. Frade, *J. Electroceram.*, 2007, **18**, 205.
- 27 T. Ishihara, J. Kilner, M. Honda and Y. Takita, *J. Am. Chem. Soc.* 1997, **119**, 2747.
- 28 T. Ishihara, Y. Tsuruta, Y. Chunying, T. Todaka, H. Nishiguchi and Y. Takita, *Electrochem. Soc.Proc.*, 2001, **28**, 90.
- 29 J. Gurgul, M. T. Rinke, I. Schellenberg and R. Pöttgen, *Solid State Ionics*, 2013, **17**, 122.
- 30 S. Lütkehoff, M. Neumann, and A. Ślebarski, *A. Physical Review B.* 1995, **52**, 13808.

Graphical abstract

Ruddlesden popper type oxide of $\text{LnSr}_3\text{Fe}_3\text{O}_{10-\delta}$ ($\text{Ln}=\text{La, Pr, Nd, Sm, Eu, Gd}$) has been investigated as active cathode for solid oxide fuel cell (SOFC). Among these cathodes, $\text{PrSr}_3\text{Fe}_3\text{O}_{10-\delta}$ (PSFO10) shows high electrical conductivity and low cathodic overpotential. The maximum power density of the cell was achieved 0.51 W.cm^{-2} at 1073 K and this is comparable with that of the cell using $\text{La}_{0.6}\text{Sr}_{0.4}\text{Fe}_{0.8}\text{Co}_{0.2}\text{O}_3$ cathode. The surface exchange coefficient, k , also confirms the high activity for the dissociation of oxygen on PSFO10. Therefore, $\text{PrSr}_3\text{Fe}_3\text{O}_{10-\delta}$ is highly promising as cathode for low temperature operation SOFCs.

